IEEE Open Journal of the
Industrial Electronics Society

Received 12 April 2024; revised 30 April 2024; accepted 26 May 2024. Date of publication 29 May 2024;
date of current version 5 June 2024. The review of this article was arranged by Associate Editor Hong Li.

Digital Object Identifier 10.1109/OJIES.2024.3406732

Design and Experimental Verification of a Bidirectional EV On-Board Charger Featuring Multiphase Operation in Full Power/Voltage Ranges

HÉCTOR SARNAGO (Senior Member, IEEE) AND ÓSCAR LUCÍA (Senior Member, IEEE)

Department of Electronic Engineering, Communications, I3A, Universidad de Zaragoza, 50009 Zaragoza, Spain

CORRESPONDING AUTHOR: ÓSCAR LUCÍA (e-mail: olucia@unizar.es)

An earlier version of this paper was presented at the at the IEEE CPE/Powereng conference, received the Conference Best Paper Award, 2023 [DOI:10.1109/CPE-POWERENG58103.2023.10227458]. This work was supported by Projects TED2021-129274B-I00, CNS2023-144980, and PDC2023-145837-I00 co-funded in part by the MICIU/AEI /10.13039/501100011033, in part by the ERDF A way of making Europe, in part by the European Union NextGenerationEU/PRTR, and in part by the DGA-FSE .

ABSTRACT Modern electric vehicles require power electronic systems capable of operating under a wide variety of operating conditions, including on-board chargers (OBCs) and dc–dc converters. These systems must function across a wide range of parameters, such as phase number, input voltage, and output battery voltage. Considering modern design standards, achieving a high-performance implementation featuring high efficiency and low cost is also mandatory, adding additional technical challenges. To address these challenges, this article proposes a novel OBC architecture designed to operate in both three-phase and single-phase configurations across the full output power range. This is achieved without requiring additional power components or degrading performance. As a consequence, the proposed solution is a universal-charging single-power-processing block that features a cost-effective implementation while achieving high power density and efficiency. In this article, a bidirectional 11-kW 800-V-battery-voltage prototype of the system is designed and constructed for a 400-V (line-to-line) mains supply.

INDEX TERMS Electric vehicle (EV), multiphase systems, on-board charger (OBC), power electronics.

I. INTRODUCTION

Electric vehicles (EVs) play a crucial role in the electrification process, contributing significantly to the decarbonization agenda. The core component of these vehicles is the electrical battery, which efficiently and reliably provides the required energy to power the electric motors and the surrounding electronics of the vehicle. Currently, two primary power ports are being considered for powering the battery. First, the fast-charging port, designed to provide a direct power flow from the external charger to the battery dc-voltage. Power ranges from 50 to 350 kW are employed to reduce the charging time to just a fraction of an hour. Second, a versatile low-power (6.6–22 kW) ac port is also integrated into the vehicle to facilitate charging from nearly any grid distribution, thus promoting the widespread adoption of EVs. This converter, known as the on-board charger (OBC) [2], [3], serves two main functions: first, to provide power access to any distribution grid, regardless the phase configuration, e.g., single-phase, split-phase, or three-phase, with voltages ranging from 85 to 265 V rms, while considering grid frequencies from 40 to 65 Hz. Second, the OBC ensures proper isolation and voltage adaptation between the mains distribution and the EV battery for safety reasons.

In recent years, a significant number of technical and review papers have studied the most effective implementations for OBCs [2], [4], [5], [6], [7]. All these papers highlight the necessity for highly versatile converters able to operate in a wide range of voltage/power levels. Moreover, in recent years, the interest in multiphase and bidirectional implementations [8], [9] has significantly increased. In order to accomplish

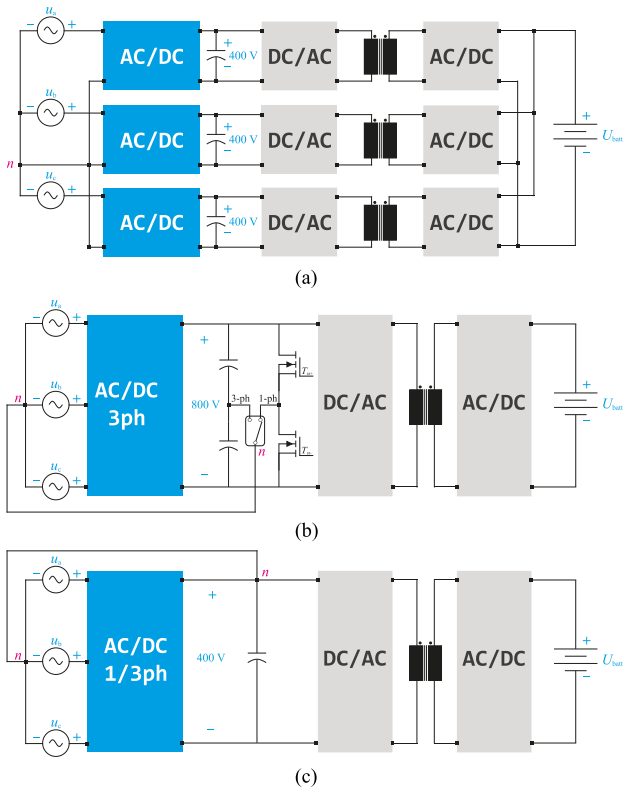

FIGURE 1. **Bidirectional OBC charger architectures achieving a unity power factor consist of an ac–dc front-end and a back-end isolated dc–dc converter. (a) Phase modular (3 × 400 V) and (b) single (800 V) front-end stage architectures that convert three-phase ac voltages u_a, u_b, u_c (or conversely, a single-phase voltage u_{abc}) to an isolated dc output voltage U_{batt}. (c) Proposed single-/three-phase single-front-end stage achieving 400 V output voltage.**

these requirements, classically a two-stage converter based on rectifier, including power factor correction (PFC) functions, and dedicated isolated dc–dc is employed [10], [11]. This solution takes the advantage of the use of the well-optimized 600-V semiconductor technology [12], considering a 400 V battery technology and, typically, unidirectional power flow [see Fig. 1(a)] [13], although bidirectional implementations based on totem-pole rectifiers are also possible. This approach, however, requires three power rails for operating in a three-phase configuration, including dedicated isolating transformers and dc–dc power converters. In addition, the control architecture, sensing circuits, and power supply design are complex due to the requirements of multiple isolation barriers and power reference considerations. The combination of all these design constraints leads to performance degradation, reduced power density, and increased cost.

Moving from a single-phase to a three-phase rectifier [12], [14] enables a low component count and a huge reduction in isolation barriers and power references. In addition, a single dc–dc converter stage can be employed, increasing power density and reducing control complexity. This scenario became possible with the development of the 1200-V SiC technology, which also enables the adoption of 800-V batteries. This advancement has been made in combination with the need for bidirectional power conversion to enable OBCs that can cope with modern vehicle-to-home, vehicle-to-vehicle, and/or vehicle-to-load charging standards [14].

Despite significant advances, state-of-the-art architectures still face significant limitations when operating under a wide range of operating conditions, i.e., input and output conditions, considering that they must operate under 120 V and 230 V multiphase networks, and with different battery charge status, i.e., 550 V up to 850 V for 800 V batteries. Specifically, single-phase configuration (or split-phase operation) is challenging for three-phase rectifiers [15], as they require an additional current path [see Fig. 1(b)] and the use of high-voltage diodes or even MOSFETs in the case of bidirectional operation. This leads to lower power conversion efficiency and, consequently, requires the use of additional power electronic components compared to three-phase operation. Besides, the high intermediate dc-link voltage of these boost-type three-phase rectifiers, typically 750–850 V [16], poses additional challenges as this prevents the use of high-power-density electrolytic capacitor technology, which is usually rated only up to 450 V. As a consequence, a series connection is usually adopted, requiring additional circuitry for voltage supervision and/or balancing, and leading to a more complex and costly implementation.

Summarizing, OBCs based on single-phase rectifiers [17], [18] offer similar performance in single (or split)/three-phase operation at the cost of a downgraded power density and efficiency levels forced by the high component count and the required multiple reference levels. In contrast, the use of a single three-phase based rectifier [19] enables an increase in the power density by unifying power references. Oppositely, single-phase operation requires additional power electronics, leading to a decrease in efficiency and, usually, power derating. In this context, this article proposes a new OBC architecture based on integrated single-phase rectifiers [1], having the benefit of the identical single/three-phase operation while having a single common-ground reference, yielding to a compact and cost-optimized implementation and with no required additional power devices or penalties in the device stress [20]. In additional, the 400 V intermediate dc-link voltage simplifies the use of electrolytic capacitor technology to decouple the grid power pulsation in single-phase operation. Then, a full-bridge-based dual-active bridge (DAB) [21] completes the OBC to provide isolation, to adapt the intermediate dc-link voltage to the battery voltage U_{batt}, and to enable a fully bidirectional operation.

The rest of this article is organized as follows. Section II details the proposed OBC architecture, describing the rectifier operation in three-phase and single-phase configuration and the operation of the isolated dc–dc converter. Section III details the control strategy to achieve versatile operation, while Section IV analyzes the proposed topology to extract the main design equations and component ratings. Section V summarizes the main implementation and experimental results and Section VI discusses the benefits of the proposed

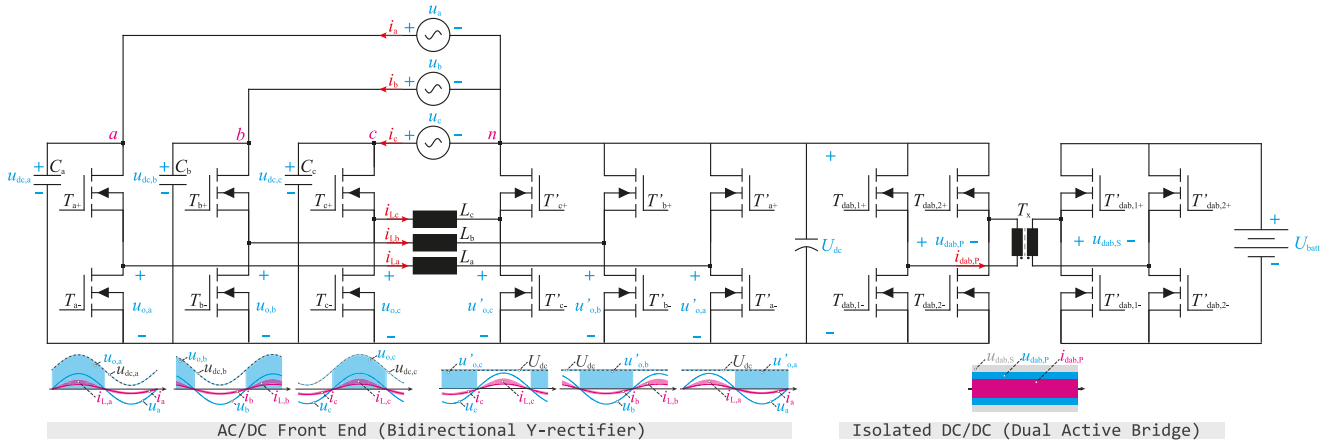

FIGURE 2. **Proposed bidirectional OBC architecture in three-phase operation including the main high-frequency waveforms during a grid cycle.**

converter compared with state-of-the-art alternatives. Finally, Section VII concludes this article.

II. OPERATIONAL PRINCIPLE

A. PROPOSED CONVERTER

This section details the proposed power converter. In order to provide a versatile solution that enables to cope with wide mains variations, to adapt the battery voltage and to ensure isolation, a two-stage architecture is selected. First, a bidirectional single-/three-phase ac–dc front-end [20] is proposed to ensure proper mains power consumption. Second, an isolated DAB dc–dc converter is utilized to ensure isolation and to accommodate battery voltage variations. The former is shown in Fig. 2, including the main converter operating waveforms for three-phase operation.

B. AC–DC FRONT-END

In this article, a differential rectifier is proposed based on the concept of the phase-modular buck–boost Y-rectifier [22]. This converter uses three identical input stages, where each one includes a buck–boost dc–dc converter connected to a common star "Y" point provided by the positive dc-link rail. This configuration results in a differential rectifier that has comparable voltage and current stress in both three- and single-phase operation. As it is described in [20], the grid neutral point n is connected to the positive intermediate dc-link rail U_{dc}. In this configuration, each phase is composed of a half-bridge leg in the ac side, connected to the corresponding grid terminal (which shows a positive voltage against the Y-rail), and a dc-side half-bridge leg, connected to the positive dc output rail (and hence also to the grid neutral point). This configuration advantageously allows both three- and single-phase operation with no additional elements required. Reconfiguration is done using relays with no impact on the power range or semiconductors usage. When using three-phase operation [see Fig. 4(a)], grid-phase voltages, u_a, u_b, and u_c, are connected to the ac-side terminals a, b, and c, respectively, and the converter provides sinusoidal grid currents i_a, i_b, and i_c in phase with the respective grid voltages.

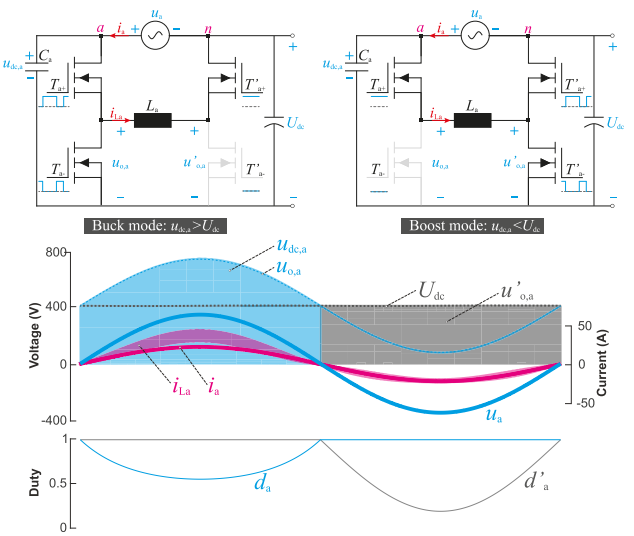

FIGURE 3. **Operating modes of the ac–dc front-end module a (top), and corresponding converter waveforms (middle), and modulation parameters (bottom).**

The operating concept of this converter is the same for all phases. For the sake of simplicity, it is explained for phase a, as depicted in Fig. 3, and the equivalent operation occurs for the remaining phases. The converter is composed of the ac- and dc-side half-bridge transistors T_{a+}, T_{a-}, and T'_{a+}, T'_{a-}, respectively. In this configuration, two different and complementary operating modes are present within one grid period.

a) *Mode I:* When the grid voltage is positive, $u_a > 0$, the ac-side half-bridge transistors T_{a+}, T_{a-}, are complementary switched and T'_{a+} is continuously activated. Considering that the converter switching frequency is much higher than the grid frequency, $f_{sw} \gg f_{ac}$, the corresponding ac-side half-bridge duty cycle, d_a, is

$$d_a(t) = \begin{cases} \frac{U_{dc}}{U_{dc}+u_a(t)}, & u_a \geq 0 \\ 1, & u_a < 0 \end{cases} \quad (1)$$

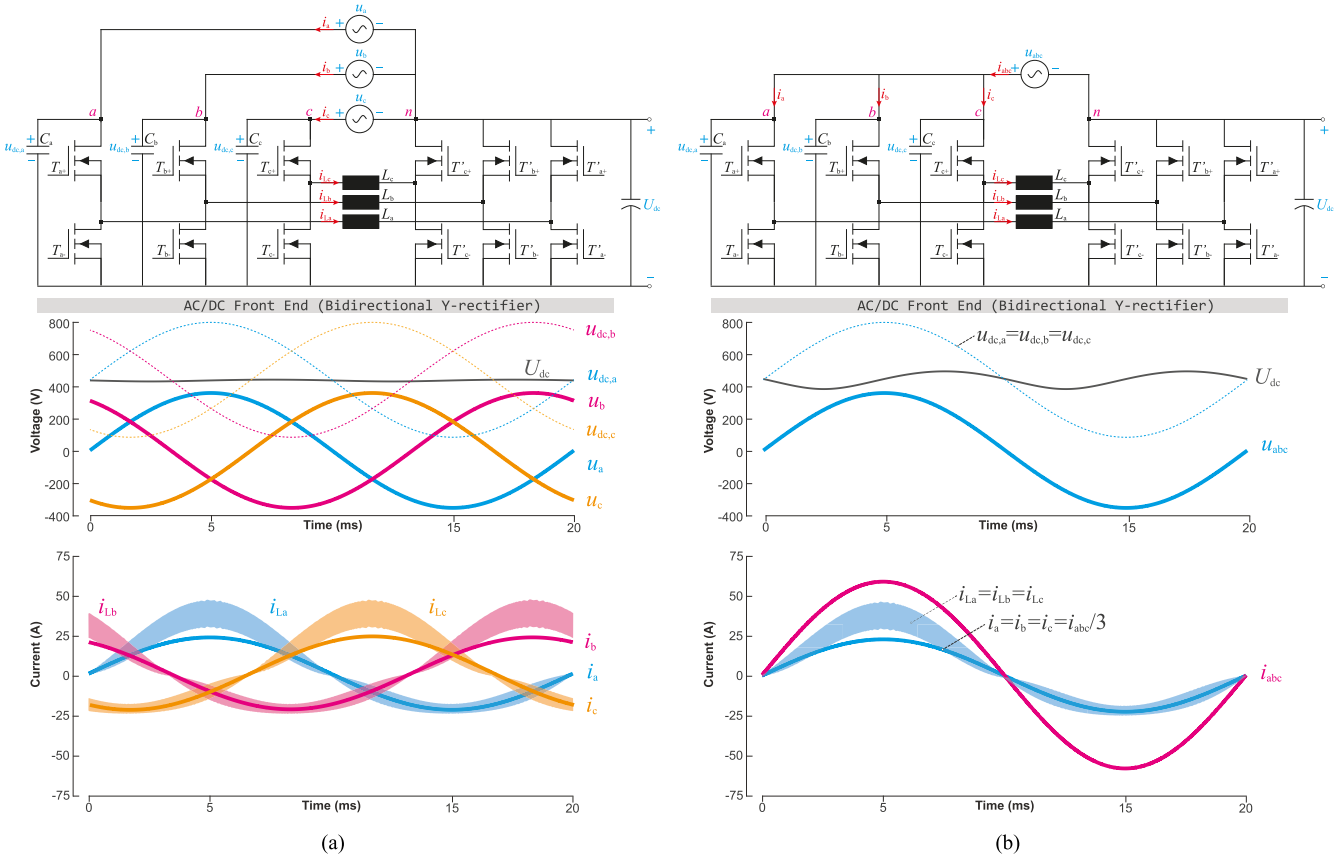

FIGURE 4. Proposed bidirectional OBC architecture including the main grid voltage and current waveforms for (a) three-phase operation and (b) single-phase operation.

where the input capacitor voltage of the ac-side half-bridge is the sum of the intermediate dc-link voltage and the grid-phase voltage, $u_{dc,a} = U_{dc} + u_a$. In order to ensure proper converter operation, a strictly positive input capacitor voltage is required, $u_{dc,a} > 0$, resulting in $U_{dc} = 400$–450 V, for universal grid operation with a wide grid line-to-neutral root-mean-square (RMS) voltage range of $U_{ac} = 85$–$265\,V_{RMS}$. As a consequence of this, 600-V rated power devices can be used for the dc-side half-bridge legs, whereas 1200 V SiC MOSFETs are required for the ac-side half-bridge legs ($U_{dc,a,max} = U_{dc} + U_{a,pk} = 520$–$825$ V), independently of the operation in single-phase or three-phase mode.

b) *Mode II:* Conversely, when the grid voltage is negative, $u_a < 0$, the converter operates in a second mode by switching the dc-side half-bridge MOSFETs T'_{a+}, T'_{a-}, with the upper transistor of the ac-side half-bridge T_{a+} continuously activated. In this case, the resulting dc-side half-bridge duty cycle, d'_a, is

$$d'_a(t) = \begin{cases} 1, & u_a \geq 0 \\ \frac{U_{dc}+u_a(t)}{U_{dc}}, & u_a < 0. \end{cases} \quad (2)$$

Fig. 3 shows the applied duty cycles that result in a mutually exclusive high-frequency switching operation of the ac- and dc-stages, such that only three out of the six half-bridges are switched simultaneously in the entire ac–dc front-end. As a consequence of this, switching losses are significantly reduced.

Finally, it is important to note that, in contrast to the phase-modular buck–boost Y-rectifier [22], the proposed converter advantageously connects the grid neutral point n with the intermediate dc-link bus, U_{dc}. This implies that in the case of single-phase connection [see Fig. 4(b)], the grid voltage u_{abc} is connected to the parallel-connected ac-side terminals a, b, and c such that the current is equally shared among the phase modules. The aforementioned connection of the grid neutral point and the positive intermediate dc-link creates a return path for the single-phase grid current i_{abc}. This represents one of the main advantages of the proposed converter over previous proposals, since it allows full output power range operation in both three-phase and single-phase operation without overdimension of power devices or requiring additional elements. Besides, both ac- and dc-side half-bridge legs are referenced to the same point, simplifying the isolation considerations and control architecture.

C. DAB DC–DC CONVERTER

The proposed OBC power converter features a back-end dc–dc converter composed of a single DAB dc–dc converter that

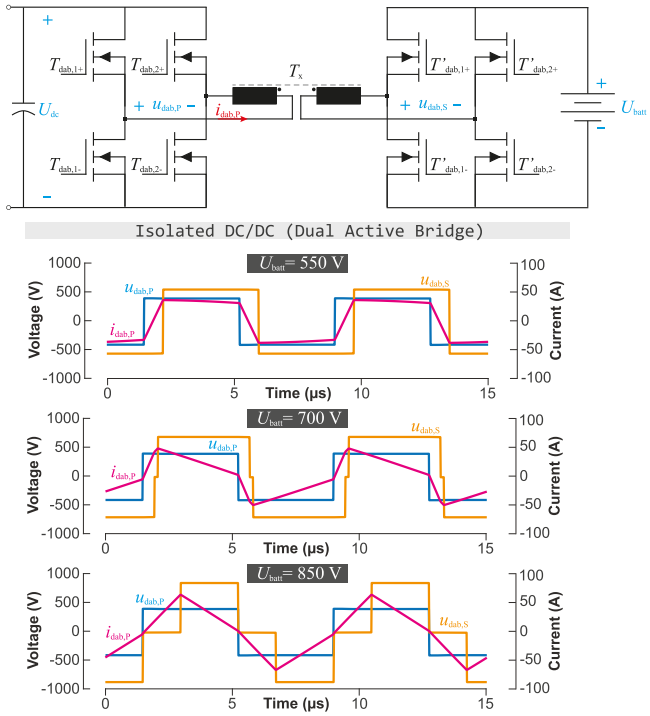

FIGURE 5. Operating modes of the dc–dc back-end module a (top), and corresponding converter waveforms (bottom).

also provides isolation through a high-frequency transformer. This converter is composed of a primary-side full-bridge, and a secondary-side full-bridge, featuring a modulation strategy that allows bidirectional power transfer and also adapts the operating conditions to the battery voltage. As a consequence of this, when compared to the state-of-the-art modular approach [see Fig. 1(a)], the proposed converter uses a single dc–dc converter to perform the required isolated power conversion, reducing the number of required power devices, magnetic components, and consequently further simplifying the isolation and control architecture.

Finally, in order to accommodate the 400 V intermediate dc-link voltage to a wide range of operating voltages typical of 800-V batteries, i.e., $U_{\text{batt}} = 550$–850 V, $n = 1.34$ has been selected as the optimum turns ratio for the transformer. In these conditions, pseudotrapezoidal control mode is used in the low-battery voltage range, achieving minimized conduction power losses for the most current-demanding operating conditions, i.e., battery fully discharged. Besides, full-ZVS soft-switching operation is ensured in both primary- and secondary-side full bridges. In addition to this, to minimize power loss in the medium-to-high battery voltage range, secondary duty cycle modulation is also applied, as described in [23] to achieve an optimal modulation profile. All these modulations profiles have been depicted in Fig. 5.

III. CONTROL STRATEGY

To operate effectively across a diverse set of conditions, ensuring sinusoidal input current consumption, and smooth battery current, three control loops have been integrated. These loops ensure proper operation of the converter, maintaining a constant battery current, either positive or negative, fed by a scaled mains-voltage current level and, consequently, in phase with the mains voltage (refer to Fig. 6). An field programmable gate array (FPGA) from AMD/Xilinx has been selected as the digital control platform, ensuring accurate control loop execution and precise pulsewidth modulation generation.

First, "Control Loop A" achieves power balance between the mains and the battery power consumption via the dc-link capacitor voltage stabilization. The dc-link voltage, U_{dc}, is measured and its peak value, $U_{\text{dc,peak}}$, is calculated twice each mains period. This value is then compared with the desired dc-link voltage, i.e., 400 V in order to provide input to a proportional-integral (PI) controller. The PI controller is executed at both the positive and negative zero crossings of the mains waveform, thereby achieving the required mains rms current level, $I_{\text{ac,rms}}$ to balance power consumption.

The proper instantaneous mains current consumption, in phase with the mains voltage, is ensured by "Control Loop B." Three identical modules of this loop, each one corresponding to a mains phase, run in parallel at the end of the switching period. The necessary duty cycles for the equivalent buck–boost stages of the rectifier are determined as the sum of the output from the "MATH" unit, which essentially computes (1) and (2), and the contribution from a PI controller. This combined effort ensures the appropriate instantaneous mains current level.

The third control loop, referred to as "Control Loop C," is crucial to maintain the required battery current level, $I_{\text{bat,OBJ}}$. A PI controller, executed once per switching period, is employed to compensate for variations in the dc-link voltage and to guarantee the desired constant current delivered to the battery. To determine the most suitable modulation strategy, a lookup table named "DAB LUT" is used. This strategy selection relies on inputs, such as the dc-link voltage, battery voltage, and the required gain, K_{DAB}.

IV. ANALYSIS

This section analyzes the main converter equations and allows us to establish the key component stress of the converter; it is divided in the rectifier stage (ac–dc) and the dc–dc converter.

A. AC–DC FRONT-END

The operating mode is equivalent for all the phase modules a, b, c and, consequently, for the sake of simplicity, it is explained only for phase a. The power processed by each phase $P_{\text{a}} = \frac{1}{2}\hat{U}_{\text{ac}}\hat{I}_{\text{ac}}$ (equal to $\frac{1}{3}$ of the total input power P_{abc}) undergoes processing through two half-bridge stages: the buck, $T_{\text{a}+}$, $T_{\text{a}-}$, and the boost, $T'_{\text{a}+}$, $T'_{\text{a}-}$, respectively. In this configuration, the input capacitor C_a, serving filtering and commutation purposes, is positioned in the buck half-bridge. According to Kirchhoff's voltage law, its time-domain voltage is given by

$$u_{\text{dc,a}}(t) = u_{\text{a}}(t) + U_{\text{dc}}. \tag{3}$$

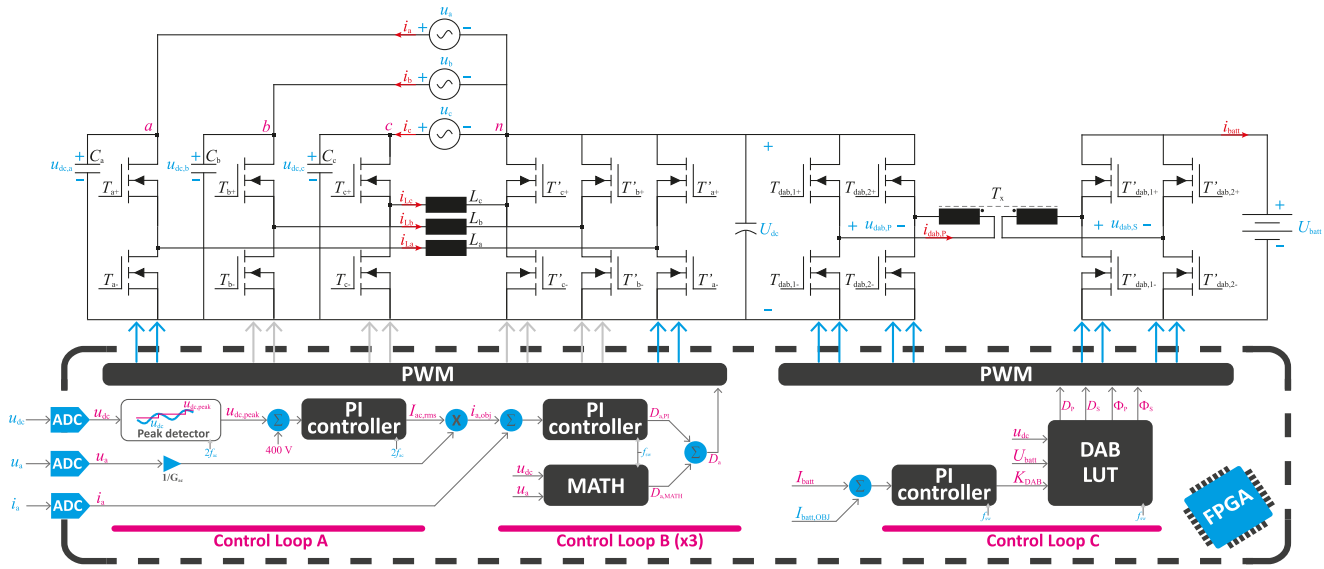

FIGURE 6. Proposed control architecture.

To prevent short-circuiting through the antiparallel diodes of the buck-side switches, T_{a+}, T_{a-}, the input stage voltage $u_{dc,a}$ must be strictly positive. The ac operation of the phase module is enabled by the *differential* interaction of the positive voltages $u_{dc,a}$ and U_{dc}, leading to the nomenclature *differential* rectifier [24]. The specific requirement of $u_{dc,a} > 0$ and (3) effectively limits the dc output voltage to values above the grid line-to-neutral amplitude

$$U_{dc} > \hat{U}_{ac}. \tag{4}$$

This limitation is equivalent to the operating limit of a standard boost-type single-phase PFC rectifier, representing a constraint compared to the standard Y-rectifier, which can generate any $U_{dc} > 0$. Note that (4) applies to both single- and three-phase operation of the proposed converter, and it is compatible with the specified $U_{dc} = 400\,\text{V}$ and $\hat{U}_{ac} = 325 V_{pk}$ of the European grid.

Neglecting the low-frequency input capacitor C_a current, the local average current in a switching period $T_s = 1/f_s$ through the inductor $\langle i_{La} \rangle$ can be expressed as follows:

$$\langle i_{La} \rangle(t) = \begin{cases} (1 + \frac{u_a(t)}{U_{dc}}) i_a(t) = \frac{i_a(t)}{d_{AI}(t)}, & u_a \geq 0 \\ i_a(t), & u_a < 0. \end{cases} \tag{5}$$

Consequently, assuming lossless operation and unity power factor, for a phase power $P_a = U_{ac} I_{ac}$, the low-frequency rms component of the inductor current flowing through the half-bridge branches is given by

$$\langle I_{La} \rangle_{RMS} = \frac{I_{ac}}{U_{dc}} \sqrt{U_{dc}^2 + \frac{3}{4} U_{ac}^2 + \frac{8\sqrt{2}}{3\pi} U_{dc} U_{ac}}. \tag{6}$$

This current is approximately 40% higher than the grid rms current I_{ac} for the specified $U_{ac} = 230\,\text{V}_{RMS}$ and $U_{dc} = 400\,\text{V}$. Note that $\langle I_{La} \rangle_{RMS}$ is identical in both three-phase and single-phase operation for a given power and grid voltage level. Another important figure of merit for the converter is the required semiconductor blocking voltage. For the buck half-bridge T_{a+}, T_{a-}, the maximum voltage is defined by $U_{an,max} = U_{dc} + \hat{U}_{ac} = 725\,\text{V}$, requiring 1200 V power semiconductors to ensure sufficient blocking voltage margin during switching transients. Alternatively, the three-level flying capacitor ac-stage structure from [25] would allow the use of high-performance and cost-effective 600 V semiconductors. In contrast, the voltage stress in the dc-side half-bridge branches is equal to the converter output voltage, $U_{dc} = 400\,\text{V}$, allowing for the use of 600 V semiconductors. A notable result and benefit of the proposed topology are the equal voltage stress outcomes in both three-phase and single-phase operation, provided that the line-to-neutral (rms) voltage U_{ac} remains constant.

B. DAB DC–DC CONVERTER

The voltage stress of the DAB full-bridges are directly the dc-link voltage, U_{dc}, and the battery voltage, U_{batt}, for the primary and the secondary sides, respectively. Assuming a lossless operation, the rms output current through the primary-side full bridge can be expressed as

$$I_{dab,P,RMS} = k_{DAB} \frac{P_{abc}}{U_{dc}} \tag{7}$$

being the DAB modulation constant $k_{DAB} = 2/\sqrt{3}$ in the case of a triangular modulation, and $k_{DAB} > 1$ for other modulations. The main semiconductor stress expressions are summarized in Table I.

V. IMPLEMENTATION AND EXPERIMENTAL RESULTS

In the context of this research and to verify the proper converter operation, a 11-kW bidirectional prototype has been designed and implemented featuring an input voltage range

TABLE 1. Key Semiconductor Stress

Component designator	Voltage stress (PEAK)	Current stress (rms)
$T_{a+}/T_{a-}, T_{b+}/T_{b-}, T_{c+}/T_{c-}$	$U_{dc} + \hat{U}_{ac}$	$\frac{I_{ac}}{U_{dc}}\sqrt{U_{dc}^2 + \frac{3}{4}U_{ac}^2 + \frac{8\sqrt{2}}{3\pi}U_{dc}U_{ac}}$
$T'_{a+}/T'_{a-}, T'_{b+}/T'_{b-}, T'_{c+}/T'_{c-}$	U_{dc}	$\frac{I_{ac}}{U_{dc}}\sqrt{U_{dc}^2 + \frac{3}{4}U_{ac}^2 + \frac{8\sqrt{2}}{3\pi}U_{dc}U_{ac}}$
$T_{dab,1+}/T_{dab,1-}, T_{dab,2+}/T_{dab,2-}$	U_{dc}	$k_{DAB}\frac{P_{abc}}{U_{dc}}$
$T'_{dab,1+}/T'_{dab,1-}, T'_{dab,2+}/T'_{dab,2-}$	U_{batt}	$k_{DAB}\frac{P_{abc}}{nU_{dc}}$

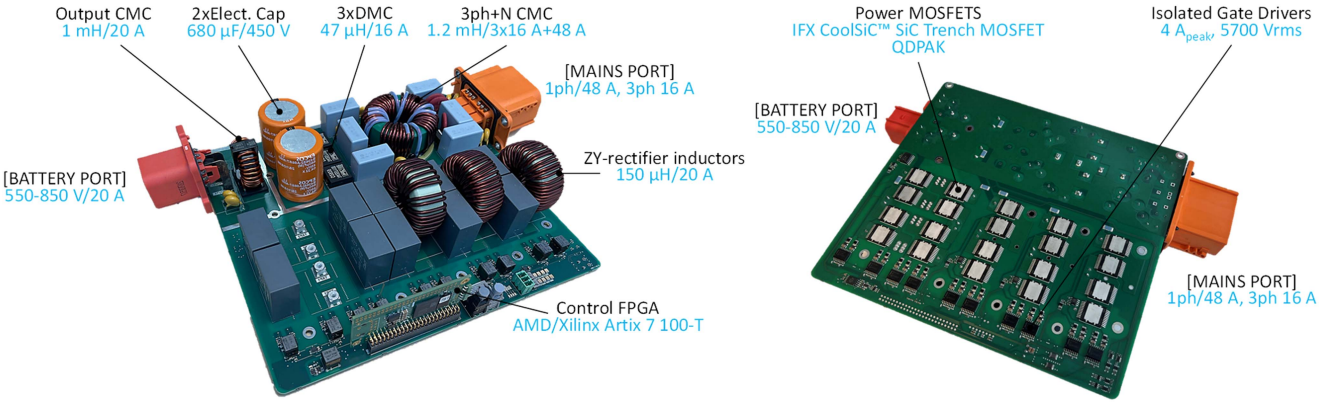

FIGURE 7. Proposed converter prototype including the main active and passive components: (a) Top and (b) bottom views.

of $U_{ac} = 85$–$265\ V_{RMS}$ (phase voltage) in both three-/single-phase operation. The back-end DAB dc–dc stage has been designed to supply 800 V high-voltage batteries with a voltage ranging from 550 to 850 V. The designed prototype features 1200 V and 750 V trench MOSFETs devices from Infineon in the rectifier stage. The DAB converter is implemented using 16 mΩ 750 V SiC MOSFET in the primary-side and 20 mΩ 1200 V SiC MOSFETs in the secondary-side stage. In order to ensure proper thermal management, all these devices are top side cooled featuring QDPAK package for a better performance.

Input capacitors C_a, C_b, and C_c are implemented using 7 μF/900V FILM capacitors to achieve a cost-effective implementation. A 300 μH inductors L_a, L_b, and L_c are implemented using Fe–Ni dust core material to obtain a compact and efficient implementation.

The power converter is digitally controlled by using an FPGA (Artix 7-100 T from Xilinx). Fig. 7 shows the implemented prototype, not including the DAB converter transformer, which is externally connected, whose dimensions are $239 \times 216 \times 58\ mm^3$ ($3.0\ dm^3$, $3.7\ kW/dm^3$, $60\ W/in^3$).

To achieve a balanced tradeoff between power losses and volume, a switching frequency of 50 kHz is selected for the ac–dc front-end (hard-switched) and a 100 kHz for the dc–dc back-end (soft-switched). Finally, further experimental measurements in the ac–dc front-end have been performed to show the efficiency of this block at 100 kHz, enabling the possibility of using the same frequency in the whole converter, at the cost of Õ.7% additional power losses.

The ac–dc front-end converter has been tested at a switching frequencies of 50 kHz and 100 kHz to verify its correct operation and perform an efficiency analysis. Fig. 8 shows the main experimental results of the proposed converter, illustrating the correct operation of the ac–dc front-end operating at 16 A rms input phase current at 100 kHz. (a) In these figures, the grid voltage and current, the inductor current, and the ac- and the dc-stage high-frequency switch-node voltage of phase a are represented. In addition to this, full-power operation (11 kW) is shown in Fig. 8 for three-phase (b) and single-phase (c) operation, proving the converter ability to operate in multiphase configuration without additional elements. Fig. 9 shows the input current total harmonic distortion (THD) and harmonic analysis for the most demanding situation, i.e., single-phase operation and maximum input power (11 kW). Under these conditions, THD is 1.82% and harmonics are in compliance with current standards, proving the feasibility of this proposal.

The main experimental waveforms of the DAB dc–dc converter at full power are also shown in Fig. 10 for minimum and maximum battery voltages, i.e., $U_{batt} = 550$ V (a) using a pseudotrapezoidal modulation and $U_{batt} = 850$ V (b) employing a triangular modulation. These results prove the converter ability to operate under a wide range of output voltage, i.e., battery voltage, conditions.

Finally, Fig. 11 shows the efficiency measurement results obtained in the full output power range, i.e., up to 3.6 kW per phase (a total input power of 11 kW). The considered ac–dc front-end achieves peak efficiency values above 98% and 97% for operation with 50 kHz and 100 kHz switching frequency, respectively, whereas the DAB converter efficiency is close to 98.5%. Fig. 12 shows the power loss distribution among the different active and passive components of the ac–dc

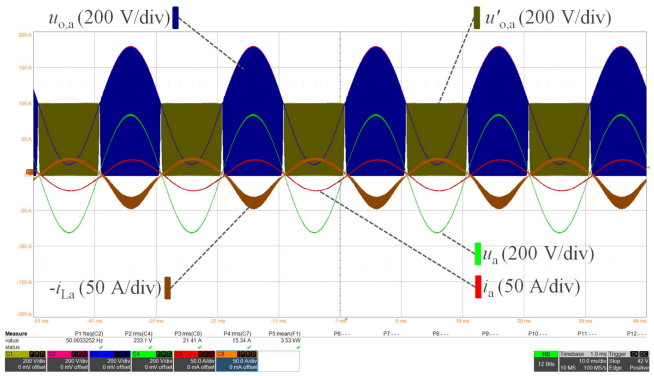

(a)

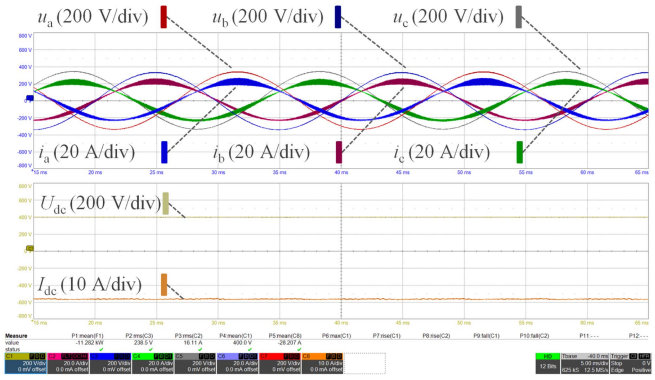

(b)

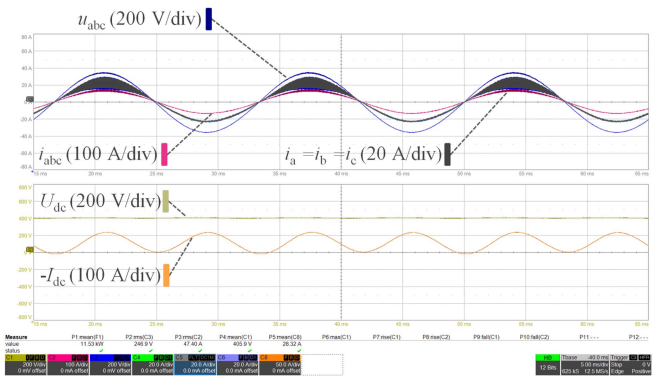

(c)

FIGURE 8. Main experimental results of the considered OBC architecture focused on the ac–dc front end. (a) Single buck–boost cell operation for $U_{ac} = 230\,V_{RMS}$ operating with 16 A input phase current at 100 kHz. From top to bottom: ac- and dc-side half-bridge switchnode voltage (200 V/div), grid voltage (200 V/div), grid current (50 A/div) and inductor current (50 A/div). (b) Three-phase operation for 400 $V_{LL,rms}$, 11 kW. (c) Single-phase operation for 240 V_{rms}, 11 kW.

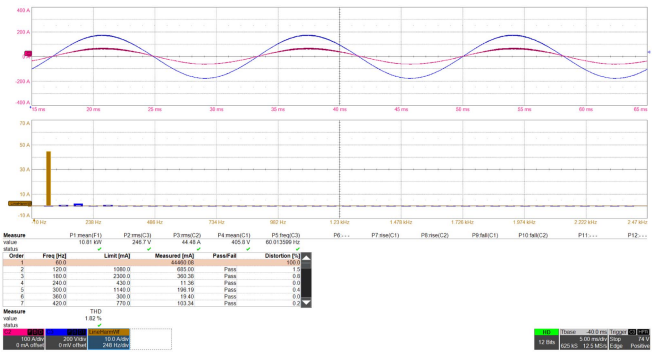

FIGURE 9. Input current THD when operating in single-phase and maximum power.

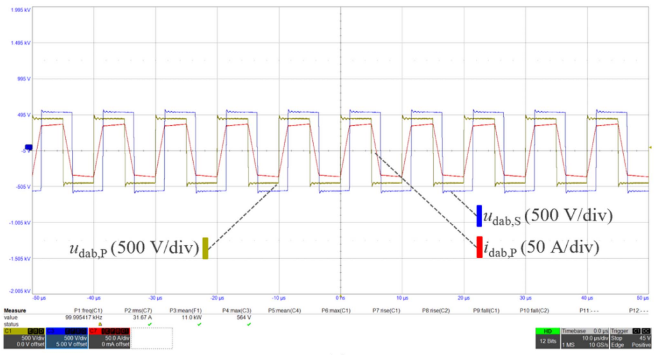

(a)

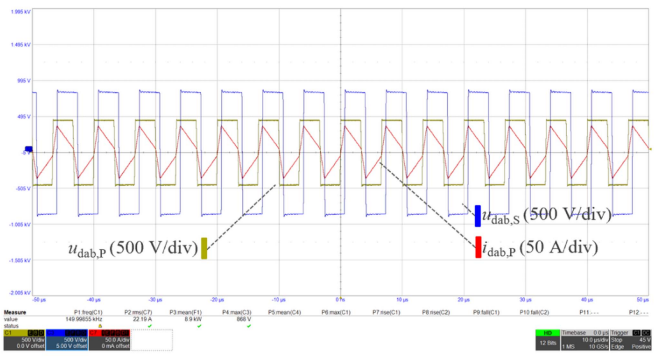

(b)

FIGURE 10. Main experimental results at maximum power (11 kW) of the back-end DAB dc–dc converter operating at (a) minimum battery voltage, $U_{batt} = 550$ V and (b) maximum battery voltage, $U_{batt} = 850$ V. Primary and secondary high-frequency DAB voltages (500 V/DIV) and primary high-frequency current (50 A/DIV) at switching frequency of 100 kHz.

front-end and dc–dc back-end converters, showing an homogeneous distribution that facilitates thermal management.

VI. DISCUSSION

This article proposes a novel OBC architecture with the main advantage of operating in both single- and three-phase modes in the entire power range without requiring additional components, and with optimized utilization of power devices. Table II provides a detailed comparison with the main state-of-the-art implementations in terms of power, efficiency, switching frequency ranges, cost, volume, and power density. As discussed in Section I, OBC converters can be categorized into two main approaches based on the ac–dc stage selection: phase modular, where a dedicated converter is required for each phase (3× ac–dc+dc–dc), and three-phase-rectifier-based, where only a single rectifier stage is required (1× ac–dc+dc–dc). The modular approaches in [17] and [18] offer high versatility, enabling operation in both single and three-phase modes with similar performance. However, this comes at the cost of increased component count and cost.

TABLE 2. Topologies Comparison

Architecture	Rated power	Efficiency	Switching frequency	Power devices	Cost[1]	Volume	Power density
Modular (3×): Totem-pole (ac–dc) + CLLC (dc–dc) [18]	6.6 kW/phase	96.5% peak (4 kW, 240 Vac to 350 Vdc)	120 kHz (ac–dc), 200-800 kHz (dc–dc)	Per rail (3×): ac–dc: 4×650V/30mOhm GaN +4×650V/25mOhm Si dc–dc: 8×650V/30mOhm GaN	38,79 €	1,73 l/rail	3,81 kW/l
Modular (3×): Unfolder (ac–dc) + DAB (dc–dc)[19]	7.2 kW/phase (20 kW total)	98% peak (20 kW, 3ph-400 Vac to 200 Vdc)	100-120 Hz (ac–dc), 500 kHz (dc–dc)	Per rail (3×): ac–dc: 4×650V/10mOhm Si, dc–dc: 32×650V/25mOhm GaN	133,89 €	2.14 l/rail	3,3 kW/l
Integrated (1×): 3ph rectifier (ac–dc) [20]	22 kW (3ph) 19.2 kW (1ph)	98.9% (22 kW, 3ph), 98.5% (19.2 kW, 1ph)	48 kHz (ac–dc)	AC–DC: 6×1200V/40mOhm SiC +6×1000V/80A Si Diodes, DC–DC: not implemented	11,49 €	3,4 l	6,4 kW/l
Proposed: Integrated (1×): Y-Rectifier (ac–dc)+ DAB (dc–dc)	11 kW (3ph) 11 lW (1ph)	97.1% (98.2% ac–dc, 98.6% dc–dc)	50 kHz (ac–dc), 100 kHz (dc–dc)	AC–DC: 6×1200V/20mOhm +6×750V/16mOhm SiC, DC–DC: 8×1200V/20mOhm SiC	25,98 €	3 l	3,7 kW/l

[1] Device cost considering 50 k units.

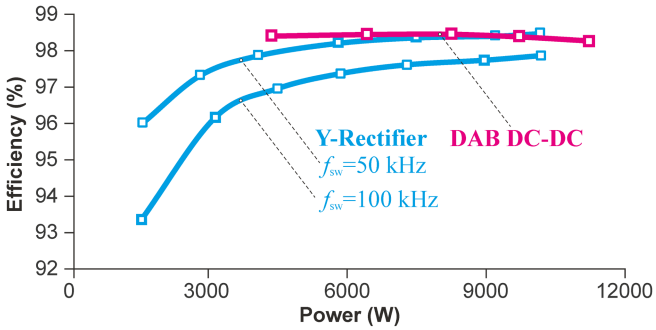

FIGURE 11. Efficiency results for both front-end rectifier and back-end dc–dc converters.

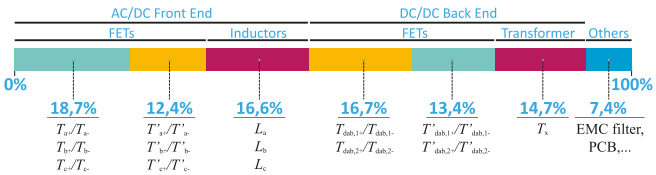

FIGURE 12. Power loss distribution at maximum output power.

For example, Lu et al. [18] utilized 32 gallium nitride (GaN) devices and 4 Si field effect transistor (FET) per rail, resulting in a device cost/kW of 133.89 €. In addition, the high-isolation requirements for powering and measuring each rail independently significantly increases the required volume, thereby reducing power density. To reduce the size of OBCs, three-phase-rectifier-based approaches are gaining popularity, requiring only a single rectifier and a dc–dc converter stage. Moreover, the combination of higher dc-link voltages, typically in the range of 750–800 V, and the maturity of SiC devices offers a cost-effective and compact solution. However, addressing the requirement for single-phase or split-phase operation with a three-phase rectifier is challenging, requiring additional power electronics for single-phase operation, and potentially reducing efficiency. For instance, in [19], where only the rectifier stage of the OBC is implemented, additional configuration relays and diodes rated up to 80 A are required for single-phase operation. Although the cost increase is not substantial, in the case of a bidirectional OBC implementation, replacing these diodes with switches would significantly increase both cost and losses. Moreover, this additional power electronics remains unused in three-phase operation, thus, not contributing to the overall converter performance. Finally, the proposed approach is based on a novel rectifier concept, combining the key benefits of previous approaches: the versatility to operate inherently in both single- and three-phase modes and the simplicity and compactness of a single converter structure. As summarized in Table II, the proposed solution features a very low device cost per kW, surpassed only by the integrated OBC approach described in [19]. However, it is important to note that only the rectifier stage is implemented, i.e., the dc–dc stage is not considered in the cost. In terms of efficiency, the proposed converter achieves levels of over 98% in both stages, with no significant difference observed between single-phase and three-phase operation. Moreover, the proposed converter achieves a high power density (3.7 kW/l), surpassing state-of-the-art implementations such as the 3.3 kW/l in [18]. It should be noted that the 3.81 kW/l described in [18] is expected to decrease if a complete OBC is implemented (as only a single rail is considered), and the 6.4 kW/l of [19] only considers the rectifier stage. Additional considerations of the implementations described in Table II should be taken into account: The modular approach [17] contains only a single rail, whereas the modular approach [18] does not decouple low-frequency current ripple in the battery side. In summary, the proposed OBC architecture offers an excellent tradeoff between cost and performance, device usage, and control complexity well suited to modern requirements.

VII. CONCLUSION

Modern EVs rely on the use of highly efficient and versatile OBC that are required to operate under a wide range of operating conditions while achieving compact and cost-effective implementations. The new requirements in terms of multiphase and advanced power flow control, i.e., single- and three-phase nominal power operation and bidirectional operation, as well as the transition toward higher voltage batteries, bring new challenges to this field. This article presents a new power conversion architecture for OBCs composed of a boost-type single-/three-phase front-end converter based on the buck–boost Y-rectifier and a DAB dc–dc converter. The proposed OBC architecture overcomes previous limitations and provides full output power range both in

three-phase and single-phase operation without requiring additional elements or power component overdimensioning. Besides, the considered architecture provides additional benefits in terms of cost, control, and electromechanical integration due to the single-stage implementation and simplification in terms of isolation and control architectures. The proposed concept has been tested using an 11-kW bidirectional three-/single-phase OBC, thereby proving the feasibility of the system approach in a wide range of operating conditions and efficient operation in the full output power range.

REFERENCES

[1] H. Sarnago, O. Lucia, D. Menzi, and J. Kolar, "Single-/three-phase bidirectional EV on-board charger featuring full power/voltage range and a cost-effective implementation," in *Proc. IEEE 17th Int. Conf. Compat., Power Electron. Power Eng.*, 2023, pp. 1–6.

[2] M. Yilmaz and P. T. Krein, "Review of battery charger topologies, charging power levels, and infrastructure for plug-in electric and hybrid vehicles," *IEEE Trans. Power Electron.*, vol. 28, no. 5, pp. 2151–2169, May 2013.

[3] H. Sarnago and O. Lucía, "Optimized EV on-board charging power converter using hybrid DCX-DAB topology," in *Proc. IEEE Appl. Power Electron. Conf. Expo.*, 2024, pp. 1305–1309.

[4] H. Wouters and W. Martinez, "Bidirectional onboard chargers for electric vehicles: State-of-the-art and future trends," *IEEE Trans. Power Electron.*, vol. 39, no. 1, pp. 693–716, Jan. 2024.

[5] M. Y. Metwly, M. S. Abdel-Majeed, A. S. Abdel-Khalik, R. A. Hamdy, M. S. Hamad, and S. Ahmed, "A review of integrated on-board EV battery chargers: Advanced topologies, recent developments and optimal selection of FSCW slot/pole combination," *IEEE Access*, vol. 8, pp. 85216–85242, 2020.

[6] S. Haghbin, S. Lundmark, M. Alakula, and O. Carlson, "Grid-connected integrated battery chargers in vehicle applications: Review and new solution," *IEEE Trans. Ind. Electron.*, vol. 60, no. 2, pp. 459–473, Feb. 2013.

[7] A. Khaligh and M. D'Antonio, "Global trends in high-power on-board chargers for electric vehicles," *IEEE Trans. Veh. Technol.*, vol. 68, no. 4, pp. 3306–3324, Apr. 2019.

[8] J. Yuan, L. Dorn-Gomba, A. D. Callegaro, J. Reimers, and A. Emadi, "A review of bidirectional on-board chargers for electric vehicles," *IEEE Access*, vol. 9, pp. 51501–51518, 2021.

[9] R. P. Upputuri and B. Subudhi, "A comprehensive review and performance evaluation of bidirectional charger topologies for V2G/G2V operations in EV applications," *IEEE Trans. Transp. Electrific.*, vol. 10, no. 1, pp. 583–595, Mar. 2024.

[10] H. Sarnago, O. Lucía, R. Jiménez, and P. Gaona, "High power density OBC featuring power pulsating buffer," in *Proc. Int. Conf. Electric Electron. Hybrid Electric Veh. Elect. Energy Manage.*, 2021.

[11] H. Sarnago and O. Lucía, "Bidirectional 400-12 V dc-dc converter with improved dynamics and integrated transformer for EV applications," in *Proc. IEEE Appl. Power Electron. Conf. Expo.*, 2024, pp. 3081–3085.

[12] H. Sarnago, O. Lucia, R. Jiménez, and P. Gaona, "Differential-power-processing on-board-charger for 400/800-V battery architectures using 650-V super junction MOSFETs," in *Proc. IEEE Appl. Power Electron. Conf.*, 2021, pp. 564–568.

[13] B. Whitaker et al., "A high-density, high-efficiency, isolated on-board vehicle battery charger utilizing silicon carbide power devices," *IEEE Trans. Power Electron.*, vol. 29, no. 5, pp. 2606–2617, May 2014.

[14] B. Li, Q. Li, F. C. Lee, Z. Liu, and Y. Yang, "A high-efficiency high-density wide-bandgap device-based bidirectional on-board charger," *IEEE Trans. Emerg. Sel. Topics Power Electron.*, vol. 6, no. 3, pp. 1627–1636, Sep. 2018. [Online]. Available: https://ieeexplore.ieee.org/document/8377992/

[15] P. Papamanolis, D. Bortis, F. Krismer, D. Menzi, and J. W. Kolar, "New EV battery charger PFC rectifier front-end allowing full power delivery in 3-phase and 1-phase operation," *Electronics*, vol. 10, no. 17, 2021, Art. no. 2069.

[16] Y. Li, J. Schäfer, D. Bortis, J. W. Kolar, and G. Deboy, "Optimal synergetic control of a three-phase two-stage ultra-wide output voltage range EV battery charger employing a novel hybrid quantum series resonant DC/DC converter," in *Proc. IEEE Workshop Control Model. Power Electron.*, 2020, pp. 1–11.

[17] T. Instruments, "GAN-based, 6,6-kw, bidirectional, onboard charger reference design," Texas Instruments, Rep. TI PMP22650, 2021.

[18] J. Lu et al., "A modular-designed three-phase high-efficiency high-power-density EV battery charger using dual/triple-phase-shift control," *IEEE Trans. Power Electron.*, vol. 33, no. 9, pp. 8091–8100, Sep. 2018.

[19] P. Papamanolis, D. Bortis, F. Krismer, D. Menzi, and J. W. Kolar, "New EV battery charger PFC rectifier front-end allowing full power delivery in 3-phase and 1-phase operation," *Electronics*, vol. 10, no. 17, 2021, Art. no. 2069. [Online]. Available: https://www.mdpi.com/2079-9292/10/17/2069

[20] H. Sarnago, O. Lucia, S. Chhawchharia, D. Menzi, and J. W. Kolar, "Novel bidirectional universal 1-phase/3-phase-input unity power factor differential AC/DC converter," *Electron. Lett.*, vol. 59, no. 13, 2023, Art. no. e12857. [Online]. Available: https://onlinelibrary.wiley.com/doi/pdf/10.1049/ell2.12857

[21] F. Krismer and J. W. Kolar, "Efficiency-optimized high-current dual active bridge converter for automotive applications," *IEEE Trans. Ind. Electron.*, vol. 59, no. 7, pp. 2745–2760, Jul. 2012.

[22] M. Antivachis, D. Bortis, L. Schrittwieser, and J. W. Kolar, "Three-phase buck-boost Y-inverter with wide DC input voltage range," in *Proc. IEEE Appl. Power Electron. Conf. Expo.*, 2018, pp. 1492–1499.

[23] F. Krismer and J. W. Kolar, "Closed form solution for minimum conduction loss modulation of DAB converters," *IEEE Trans. Power Electron.*, vol. 27, no. 1, pp. 174–188, Jan. 2012.

[24] A. Darwish, A. M. Massoud, D. Holliday, S. Ahmed, and B. W. Williams, "Single-stage three-phase differential-mode buck-boost inverters with continuous input current for PV applications," *IEEE Trans. Power Electron.*, vol. 31, no. 12, pp. 8218–8236, Dec. 2016.

[25] D. Menzi, M. Zhang, J. W. Kolar, and J. Everts, "3-ϕ bidirectional buck-boost sinusoidal input current three-level SiC Y-rectifier," in *Proc. IEEE Appl. Power Electron. Conf. Expo.*, 2021, pp. 590–598.